Combined XAFS spectroscopy and *ab initio* study on the characterization of iron incorporation by montmorillonite

11 *Annamária Kéri[1,2,*], Rainer Dähn[1], Matthias Krack[3], Sergey V. Churakov[1,2]*

12 [1]Laboratory for Waste Management, Paul Scherrer Institute, CH-5232 Villigen PSI,
13 Switzerland

14 [2]Institute of Geological Sciences, University of Bern, CH-3012 Bern, Switzerland

15 [3]Laboratory for Reactor Physics and Systems Behaviour, Paul Scherrer Institute, CH-5232
16 Villigen PSI, Switzerland

17 *Corresponding author. E-mail: annamaria.keri@psi.ch

18   Tel: +41 56 310 2368

19   Fax: +41 56 310 2199

20

21 **Abstract**

22 Iron occurs in clay minerals in both ferric and ferrous forms. Depending on its oxidation state
23 and the environmental conditions, it can participate in redox reactions and influence the
24 sorption processes at surfaces of clay minerals. Knowing the oxidation state and the
25 preferential structural position of Fe^{2+} and Fe^{3+} is essential for the detailed understanding of
26 the mechanism and kinetics of such processes. In this study, molecular dynamics (MD)
27 calculations based on density functional theory (DFT+U) were applied to simulate the
28 incorporated Fe in bulk montmorillonite and to explain the measured Fe K-edge X-ray
29 absorption fine structure (XAFS) spectra. The analysis of the experimental data and
30 simulation results suggested that iron in montmorillonite is preferentially incorporated as Fe^{3+}
31 into the octahedral layer. The simulations showed that there is no preferential occupation of
32 *cis*- or *trans*-sites by Fe^{2+} and Fe^{3+} in bulk montmorillonite. A very good agreement between
33 the *ab initio* simulated and measured XAFS spectra demonstrate the robustness of the
34 employed simulation approach.

35

1. Introduction

Iron is one of the most abundant redox-active element in soils and sediments[1]. Main phases containing ferrous and ferric iron in the sub-surface environment are oxides, hydroxides and clay minerals. Since clay minerals incorporate structural iron in both ferrous (Fe^{2+}) and ferric (Fe^{3+}) oxidation states, iron species associated with naturally occurring clay minerals are of a great relevance for bio-geochemical redox reaction, geochemical recycling of heavy metals and migration of radionuclides[1,2-5]. Accordingly, Fe-bearing clay minerals play a role in the main redox controlling phase in geochemical systems. They can concurrently act as electron donor for oxidative sorption of redox sensitive cations which affect e.g. the net negative charge of the mineral structure, the hydration of smectite surfaces and the cation exchange capacity of the clay mineral[6-8]. Wet chemistry measurements, batch sorption experiments and spectroscopy studies revealed that the adsorption of ferrous iron on clay minerals are strongly depended on the structural iron concentration and its redox state that has also an influence on the individual uptake characteristics of ferrous iron and other divalent ions when Fe-bearing clay minerals are present in the system[3,9-11]. The influence of the competitive sorption effects between Fe^{2+} and other relevant transition metals on their uptake characteristics remains an important issue[3].

The structure of Fe-bearing smectites can be described as layers of pseudohexagonally ordered sheets of alumina octahedra sandwiched between two opposing tetrahedral siloxane sheets[12]. Fe^{2+} and Fe^{3+} mainly substitutes in the Al octahedral sheet while minor quantities of Fe^{3+} can substitute for Si in the tetrahedral sheet. One third of the octahedral sites are *trans*-symmetric and two thirds of the octahedral sites are *cis*-symmetric with respect to the orientation of the hydroxyl (OH^-) groups[12,13]. Most of the Fe-bearing clay minerals belong to 2:1 type of dioctahedral smectites in which only two thirds of the possible octahedral positions are occupied[12]. Ferric and ferrous iron can occupy both the *cis-* and *trans*-sites.

A discussion about how iron is distributed between the *cis-* and *trans-* octahedral sites in 2:1 dioctahedral smectites has been going on for many years. It has been demonstrated that iron distribution in the octahedral and in the tetrahedral layer strongly depends on the total Fe content[14]. A general conclusion by Stucki[15] based on a variety of spectroscopic and structural measurements including Mössbauer and infrared spectroscopy[16] is that with increasing iron-content in the octahedral layer, the more vacant *trans*-sites are, and conversely, iron-poor clay minerals exhibit with populated *trans*-sites. The structure of the dioctahedral Fe-rich end-member, nontronite is well-studied and the relative distribution in the octahedral layer of

69 many cations (e.g. Fe^{3+}, Mg^{2+}) is quantified[5,17]. It has also been demonstrated that the

70 structurally incorporated iron takes place in the oxidative adsorption of transition metals that

71 can be reversible or irreversible depending on the alterations in the lattice structure of the

72 smectite[8,17]. Much less is known about iron distribution in low (~2-3%) Fe-bearing

73 montmorillonites, such as Milos- and Wyoming-montmorillonite. According to Stucki[15], the

74 preferred occupational site should nearly equally be distributed among the *cis-* and *trans-*sites

75 but the quantification is still lacking[18].

76 The oxidation and the reduction of structural octahedral iron has been shown to be reversible

77 in a wide range of redox conditions. Recent experimental observations demonstrated that the

78 reversible reduction and oxidation of Fe-rich and Fe-poor clays occurs at different redox

79 potentials[19,21]. Whereas nearly 100% oxidation and reduction efficiency is achieved for Fe-

80 poor montmorillonite, a noticeable amount of iron remain redox inactive[19]. Electrochemical

81 and spectroscopic analysis of the reduction and the re-oxidation cycles performed with the

82 different Fe-bearing smectites suggested that irreversible structural changes take place in the

83 clay structure during the first reduction or oxidation cycle[20].

84 Despite the large body of existing experimental work investigating the redox properties of

85 structurally incorporated iron in clay mineral lattices, the molecular-level description is still

86 lacking because the quantitative characterization of Fe^{2+} and Fe^{3+} in different structural

87 position of the clay minerals remains challenging. The origin of the difficulties is twofolds.

88 *(1)* X-ray adsorption fine structure (XAFS) and Mössbauer-spectroscopy are the two most

89 widely applied tools for the spectroscopic identification of structural Fe incorporation in clay

90 minerals[3,9,20,21,22]. The data analysis is often based on reference spectra for Fe^{2+} and Fe^{3+} end-

91 members, which, however, may represent Fe in a mixed structural state. *(2)* Iron can

92 unequally be distributed between *cis-* and *trans-*octahedral sites which can barely or not at all

93 be distinguished by these spectroscopic methods[21,22].

94 Significant advances in the theoretical description of the XAFS spectra made it possible to

95 perform theoretical prediction of extended X-ray absorption fine structure (EXAFS) and X-

96 ray absorption near edge structure (XANES) based on atomistic scale *ab initio* simulations.

97 We have recently demonstrated that the combination of EXAFS spectroscopy and *ab initio*

98 calculations allows a quantitative description of metal-uptake by clay minerals at the atomistic

99 level[23]. A similar approach was applied to investigate speciation of arsenic[24,25] and silver[26]

100 proving the applicability of this method. Studies performed on scandium and on UO_2

101 confirmed the successful application of the method to systems containing elements with

102 delocalized *f-* and *d-*electrons which are known to be challenging for *ab initio* simulations[27,28].

103 Whereas the modelling of the EXAFS spectra has nearly become a routine, the theoretical
104 simulation of XANES spectra for complex systems is still rare. Recent advances of the theory
105 and computational algorithms, made it possible to obtain accurate XANES spectrum of a
106 given structure on the basis of the exact curve-wave theory[29].

107 In this study, we demonstrate that it is possible to obtain a consistent quantitative
108 interpretation of the measured EXAFS and XANES spectra using linear combination fit of
109 spectra obtained from atomistic simulations. To this end, we obtained a set of *ab initio*
110 molecular dynamic trajectories of Fe-bearing montmorillonite with different structural
111 location of ferrous and ferric iron. We further performed a sensitivity analysis of the
112 theoretical model parameters for the XAFS spectra simulations to evaluate the effects of the
113 changing in the structural environment and the Fe oxidation state on the spectra. Comparing
114 the modelling results and the experimental observations, we gained insights into the structural
115 environment of iron. To the best of our knowledge, this is the first complete theoretical
116 evaluation of Fe K-edge XAFS modeling performed on a Fe-bearing clay mineral system.

117 **2. Materials and methods**

118 **2.1. Modeling setup**

119 In our study, we considered idealized defect free tetrahedra-octahedra-tetrahedra (TOT)
120 frames of a 2:1 dioctahedral clay with the general formula of $(4x[Al_8Si_{16}O_{40}(OH)_8])$. It is
121 often used as the simplest structural prototype for dioctahedral clays. The simulations were
122 performed on a single clay particle without water in the interlayer. The dimensions of the
123 orthorhombic supercell were $(18.2 \times 20.8 \times 15.0)$Å. Similar to the previous work[23,30], the cell
124 parameter in the "*c*" direction was fixed at 15 Å to minimize the interaction between the
125 periodic images[31,32]. The incorporation of ferrous and ferric iron in the structure was
126 considered as an exchange with the alumina in *cis-* and *trans*-octahedral position (Figure 1),
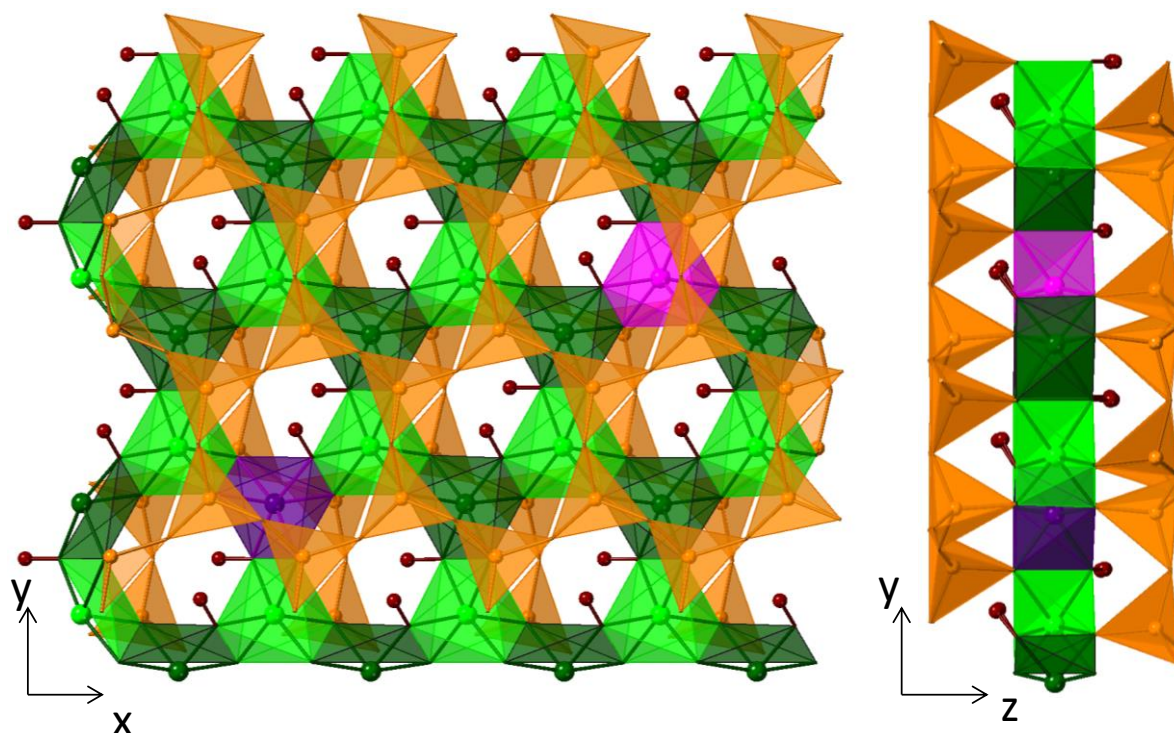127 respectively[33].

128

Figure 1. Views of the modeled montmorillonite with substituted iron at the *cis-* and *trans-*sites of the octahedra. The structural incorporation of Fe is illustrated as pink (magenta) octahedron at the *cis-*site and dark purple octahedral at the *trans-*site. The *cis-* and *trans-*site substitution can be distinguished by the different relative position of hydroxyl (OH⁻) groups shown with red spheres. Alumina octahedra are shown in green while silica tetrahedra are orange.

2.2. *Ab initio* calculations

The spin polarized electronic structure calculations were performed based on the density functional theory (DFT) using the Gaussian Plane Wave (GPW) method as it is implemented in the QUICKSTEP module of the CP2K code[34,35]. The scalar-relativistic norm-conserving pseudopotentials of Goedecker, Teter and Hutter (GTH)[36,37] were applied to avoid the explicit consideration of the core electrons (for iron [Ne] $3s^2\ 3p^6\ 4s^2\ 3d^6$). The wave functions of valence electrons were described by a linear combination of contracted Gaussian-type orbitals using MOLOPT basis sets optimized for the corresponding GTH pseudopotentials[38]. An auxiliary basis set of plane waves was employed to expand the electronic density using an electronic density cutoff of 1500 Ry for the electronic density of states calculation and 400 Ry for molecular dynamics simulations. The exchange and correlation energy was calculated using the exchange-correlation functional of Perdew, Burke and Ernzerhof (PBE)[39,40]. The simulations were performed with a multiplicity $(2S + 1)_{Fe^{2+}} = 5$ for systems with a ferrous iron and $(2S + 1)_{Fe^{3+}} = 6$ for systems with a ferric iron, respectively.

149 Conventional DFT is known to underestimate the Coulomb repulsion between the localized
150 *3d*-electrons of Fe[41]. In order to obtain a more accurate description of these states, the so-
151 called DFT+U method was applied[42,43]. In this semi empirical approach, an additional
152 potential is applied on the selected *3d*-states of Fe (for more details see Supporting
153 Information 1).

154 Born-Oppenheimer molecular dynamics (MD) simulations using a Γ-point sampling were
155 performed within the canonical ensemble (NVT) controlled by a stochastic thermostat[44]
156 employing an MD time step of 0.5 fs. In each time step, the energy was converged to
157 6.3×10^{-5} kcal/atom. In this way, four 20 ps long *ab initio* MD trajectories of montmorillonite
158 with structural Fe^{2+} and Fe^{3+} present in *trans-* and *cis*-position were obtained which were used
159 to calculate thermal averaged XAFS spectra of the Fe-bearing montmorillonite.

2.3. Calculations of EXAFS and XANES spectra

161 The EXAFS spectra were calculated based on molecular configurations derived from the *ab*
162 *initio* simulations using the FEFF 8.40 software[45,46]. For each atomic configuration, the
163 scattering potential of the atoms were calculated self-consistently[45,47]. The amplitude
164 reduction factor (S_0^2) was set to 1.0. Multiscattering paths up to eight legs with path lengths up
165 to 7.0 Å were taken into account. The radius of the cluster for self-consistent full multiple
166 scattering calculations was set to 5.0 Å.

167 The thermal disorder was taken into account in two ways. In the first case, 320 molecular
168 snapshots from MD trajectories at 300 K simulating temperature separated by a 50 fs time
169 step were averaged. Here, the thermal motion of the atoms were "directly" considered. In the
170 second "indirect" case, the static configurations derived from the initially relaxed structures
171 were used with a Debye-Waller factor of 0.006 in the EXAFS calculations. Other parameters
172 were set to the default values[46,48].

173 The calculated EXAFS spectra served as the basis for the interpretation of the experimental
174 data. The linear combination fit to the experimental EXAFS spectra was performed according
175 to Eq. 1 after max-min normalization to the value of the first oscillation of the calculated and
176 the measured spectra[23].

$$Q = \left\| k^3 \left[\sum_i \left(a_i^2 \chi_i(k) \right) - \chi^{exp}(k) \right] \right\|^2 + \left\| a_i^2 \right\|^2 \tag{1}$$

178 where $\langle \chi(k) \rangle_i$ are the calculated and $\chi^{exp}(k)$ is the experimental EXAFS spectra, a_i^2 are the
179 fitting parameters for the four different types of montmorillonite structures. The fitting was
180 limited to the interval of $k(\text{Å}^{-1}) \in [3.0, 9.0]$.

181   The theoretical prediction of XANES spectra is very challenging because of the complexity of

182   the underlying equations which can only be solved in an approximate way. The aim of this

183   study was *(1)* to demonstrate that the quantitative approach used for the interpretation of

184   EXAFS spectra is also applicable to XANES spectra; *(2)* to determine the preferred oxidation

185   state and occupational site of iron with two independent methods. The XANES spectra were

186   calculated on the basis of two different theoretical approaches. The first set of the XANES

187   spectra was obtained using the self-consistent real space multiple scattering (RSMS) method

188   implemented in the FEFF 8.40 code. The second set of XANES spectra was obtained using

189   the fully relativistic density functional theory with the local spin-density approximation (DFT-

190   LSDA) code FDMNES[49]. We calculated the spectra for 6.0 Å large molecular clusters derived

191   from the *ab initio* geometry optimization and MD simulations. The scattering potentials of the

192   atoms were calculated self-consistently (SCF) for each atomic configuration. For the

193   structures obtained by geometry optimization, the XANES spectra were obtained by

194   convolution of electronic DOS with an arctangent weighted Lorentzian as it is defined in the

195   FDMNES software[49-51]. Other parameters were set to the default values[52]. (More detailed

196   information about the FDMNES parameter choice can be found in the Supporting

197   Information 2.) For the data from MD simulations, well-converged XANES spectra were

198   obtained convolving 100 instantaneous snapshots (separated by 160 fs each).

199   The calculated XANES spectra also served as the basis for the interpretation of the

200   experimental data after max-min normalization. The fit to the experimental XANES spectra

201   was performed according to Eq. 2, which is conceptually similar to Eq. 1.

202 $$Q = \left\| \sum_i \left(b_i^2 \mu_i(E) \right) - \mu^{exp}(E) \right\|^2 + \left\| b_i^2 \right\|^2 \qquad (2)$$

203   where $\mu_i(E)$ are the calculated and $\mu^{exp}(E)$ is the experimental XANES spectra, b_i^2 are the

204   fitting parameters for the four different type of montmorillonite structures. The fitting was

205   limited to the interval of $E(\text{eV}) \in [7110, 7200]$ (the Fe K-edge is 7112 eV).

206   The Euclidian norm was used during the fittings as defined by the scalar product. The fit was

207   accepted when the spectra features in the XAFS signal matched and the Q values (indicators

208   for the fit quality) were the lowest for the given a_i^2 and b_i^2 values, respectively.

209   2.4. XAFS experiments

210   Two type of low Fe-bearing montmorillonite samples were used which show similar diversity

211   of octahedral crystal chemistry[53]. A Milos- (Mil) and a Wyoming-montmorillonite (SWy)

212   sample was prepared from the "as received" material without any physical or chemical

213   treatment by pressing a pellet. The Fe K-edge XAFS spectra were collected at the Stanford

214   Synchrotron Radiation Lightsource (SSRL, Menlo Park, CA) at the beamline 11-2 using a

215   Si(220) double crystal monochromator and a Canberra 100-pixel Ge solid-state monolith

216   detector. Higher order harmonics were rejected by detuning the monochromator by 30%. The

217   monochromator angle was calibrated at the Fe K-edge by assigning the energy of 7112 eV to

218   the first inflection point of the K-edge absorption spectrum of Fe metal foil. XAFS data

219   reduction was performed with the Athena/Artemis interface of the IFEFFIT software[54,55]

220   following standard procedures[56,57].

221   **3. Results and Discussion**

222   **3.1. EXAFS spectra**

223   The calculated Fe K-edge EXAFS spectra for montmorillonite with Fe^{2+} and Fe^{3+} located in

224   the *cis-* and *trans-*occupational sites were obtained and compared with experimental

225   spectrum. The statistical and thermal disorder was first taken into account directly as the MD

226   trajectories modeled at 300 K temperature served as the basis for the spectroscopic

227   calculations (Figure 2a). In the second case, when the relaxed atomic structures at 0 K were

228   the basis for the EXAFS calculations, a global Debye-Waller factor was applied in the

229   spectroscopic studies (Figure 2b). Although, the MD based EXAFS spectra were broadened,

230   the spectra obtained from the relaxed geometries and the MD trajectories agree very well

231   (Figure 2a,b).

232   The calculated spectra for Fe^{2+} and Fe^{3+} are clearly different in both cases. The first difference

233   between the spectra with distinct iron ionic state is a slight shift in the first oscillation at

234    $k{\sim}4.3/4.5\,\text{Å}^{-1}$. A double-bounced oscillation at $k{\sim}6.1/6.6\,\text{Å}^{-1}$ was present only for the

235   structures containing ferric iron. Differences could also be seen at the third oscillation

236   ($k{\sim}7.7/8.4\,\text{Å}^{-1}$) where the shoulders were at the opposite side (left for Fe^{2+} and right for

237   Fe^{3+}). On the other hand, iron in the *cis-* or *trans-*coordination (light and dark lines on

238   Figure 2a,b) turned out to have a minor effect on the obtained spectra.

239   The spectra of the Milos- and Wyoming-montmorillonite samples were similar, the only

240   difference appeared at the double-bounced oscillation at $k{\sim}6.1/6.6\,\text{Å}^{-1}$. The second

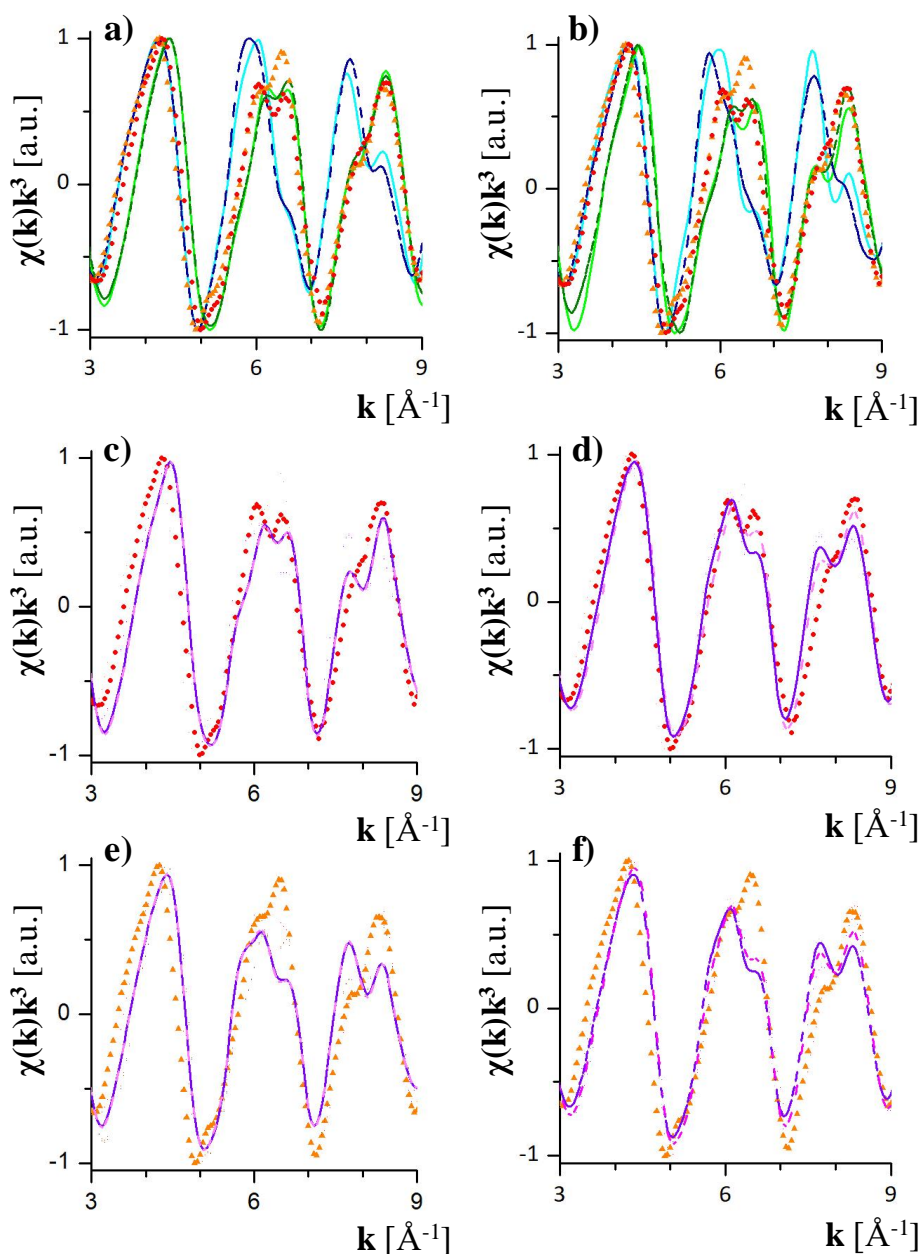241   oscillation for the SWy sample was higher.

Figure 2. Experimental EXAFS spectra (red circles for Milos- and orange triangle for SWy-montmorillonite) of montmorillonite with iron incorporation and modeled EXAFS spectra (lines) of Fe incorporated in the octahedral layer of 2:1 clay. In panels a and b, blue colors correspond to the incorporated ferrous iron (Fe^{2+}), while green colors represent incorporated ferric iron (Fe^{3+}). The lines with lighter color represent the iron at the cis-site, while dashed darker lines correspond to the trans-occupational site. In panels c−f, the lines represent the linear combination fits, the darker purple lines show "Fit 1", while the dashed lighter pink lines correspond to the "Fit 2". Panels c and d represent fits to the Milos- montmorillointe spectra with contributions determined in Table 1, while panels e and f show linear combination fits for SWy-montmorillonite spectra with contributions determined in Table 2. The calculated EXAFS spectra for panels a, c, and e were derived from MD simulations, while in panels b, d, and f, the relaxed structures served as a basis.

The qualitative comparison of the calculated EXAFS spectra and the experimental ones indicate that the iron is present mainly in the Fe^{3+} form in both Milos- and Wyoming-montmorillonite. Several linear combination fits of the measured Milos- and Wyoming-montmorillonite spectra based on the theoretical one for the Fe_{Cis}^{2+}, Fe_{Trans}^{2+}, Fe_{Cis}^{3+} and Fe_{Trans}^{3+} were performed, in order to obtain a quantitative estimation of the preferential occupational sites and the iron oxidation state. The best linear combination fits ("*Fit 1*" in Table 1 and 2) obtained based on the MD trajectories and the relaxed structures are compared with the experimental data in Figure 2c-f. The best agreement ("*Fit 1*") could be obtained for weighted spectra containing of Fe^{2+} (30-40%) and Fe^{3+} (60-70%). Iron was found to be preferentially in ferric form in both Milos- and Wyoming-montmorillonite that agreed with the assumption of earlier studies[9,53,58]. The differences in the quality of the fits between the Milos- and Wyoming-montmorillonite can be explained by the different distribution of the Fe atoms in the structure. The Fe^{3+} atoms are randomly distributed in Milos-montmorillonite, while Wyoming-montmorillonite displays an ordered iron distribution[53]. The simulations were performed at low Fe concentration without considering iron-iron clustering. The iron-iron clustering is believed to be responsible for the double-bounced oscillation at $k{\sim}6.1/$ 6.6 Å^{-1}, therefore could not be reproduced with the applied structural model.

The spectra of Fe_{Cis}^{2+} and Fe_{Trans}^{2+} as well as the spectra of Fe_{Cis}^{3+} and Fe_{Trans}^{3+} show only slight differences, thus a second linear combination fit ("*Fit 2*") was performed on the calculated structures. In this case, the total contributions of the Fe^{2+} and Fe^{3+} were kept the same, but the contributions of the different occupational sites were equalized (Table 1 and 2). The comparison of the fitting quality (Table 1 and 2) in and the fitted curves (Figure 2c-f) revealed that there were only small differences between the two fits. Therefore, the preferential occupation of *cis-* or *trans-*sites by Fe^{2+} and Fe^{3+} in montmorillonite could not be determined by only comparing the calculated and the measured EXAFS spectra.

280 **Table 1.** Parameters (contributions and quality (Q_{Mil})) of the EXAFS and XANES linear
281 combination fit of incorporated iron with distinct oxidation state (Fe^{2+}/Fe^{3+}) at different
282 occupational site (*cis/trans*) for Milos-montmorillonite, respectively[a].

	Basis of the EXAFS calculation	Number of the fit	Contribution [%]				Q_{Mil}^{b} [-]
			Fe²⁺		Fe³⁺		
			Cis	*Trans*	*Cis*	*Trans*	
EXAFS	**MD trajectories**	*"Fit 1"*[a]	20	12	28	40	3.31
	Figure 2b	*"Fit 2"*[a]	16	16	34	34	3.33
	Relaxed structures	*"Fit 1"*[a]	14	18	0	68	4.49
	Figure 2d	*"Fit 2"*[a]	16	16	34	34	5.20
XANES	**MD trajectories**	*"Fit 1"*[a]	0	0	100	0	0.600
	Figure 4b	*"Fit 2"*[a]	0	0	50	50	0.627
	Relaxed structures	*"Fit 1"*[a]	0	0	100	0	0.442
	Figure 4d	*"Fit 2"*[a]	0	0	50	50	0.443

[a]"*Fit 1*" corresponds to the "best fit", while "*Fit 2*" is the constrained "equal site distribution fit".
[b]Q_{Mil} is calculated using Eq. 1 for EXAFS and Eq. 2 for XANES.

283 **Table 2.** Parameters (contributions and quality (Q_{SWy})) of the EXAFS and XANES linear
284 combination fit of incorporated iron with distinct oxidation state (Fe^{2+}/Fe^{3+}) at different
285 occupational site (*cis/trans*) for SWy-montmorillonite, respectively[a].

	Basis of the EXAFS calculation	Number of the fit	Contribution [%]				Q_{SWy}^{b} [-]
			Fe²⁺		Fe³⁺		
			Cis	*Trans*	*Cis*	*Trans*	
EXAFS	**MD trajectories**	*"Fit 1"*	36	4	19	41	8.45
	Figure 2b	*"Fit 2"*	20	20	30	30	8.60
	Relaxed structures	*"Fit 1"*	13	30	0	57	10.15
	Figure 2d	*"Fit 2"*	21.5	21.5	28.5	28.5	11.22
XANES	**MD trajectories**	*"Fit 1"*	0	0	0	100	0.582
	Figure 4b	*"Fit 2"*	0	0	50	50	0.603
	Relaxed structures	*"Fit 1"*	0	0	0	100	0.389
	Figure 4d	*"Fit 2"*	0	0	50	50	0.391

[a]"*Fit 1*" corresponds to the "best fit", while "*Fit 2*" is the constrained "equal site distribution fit".
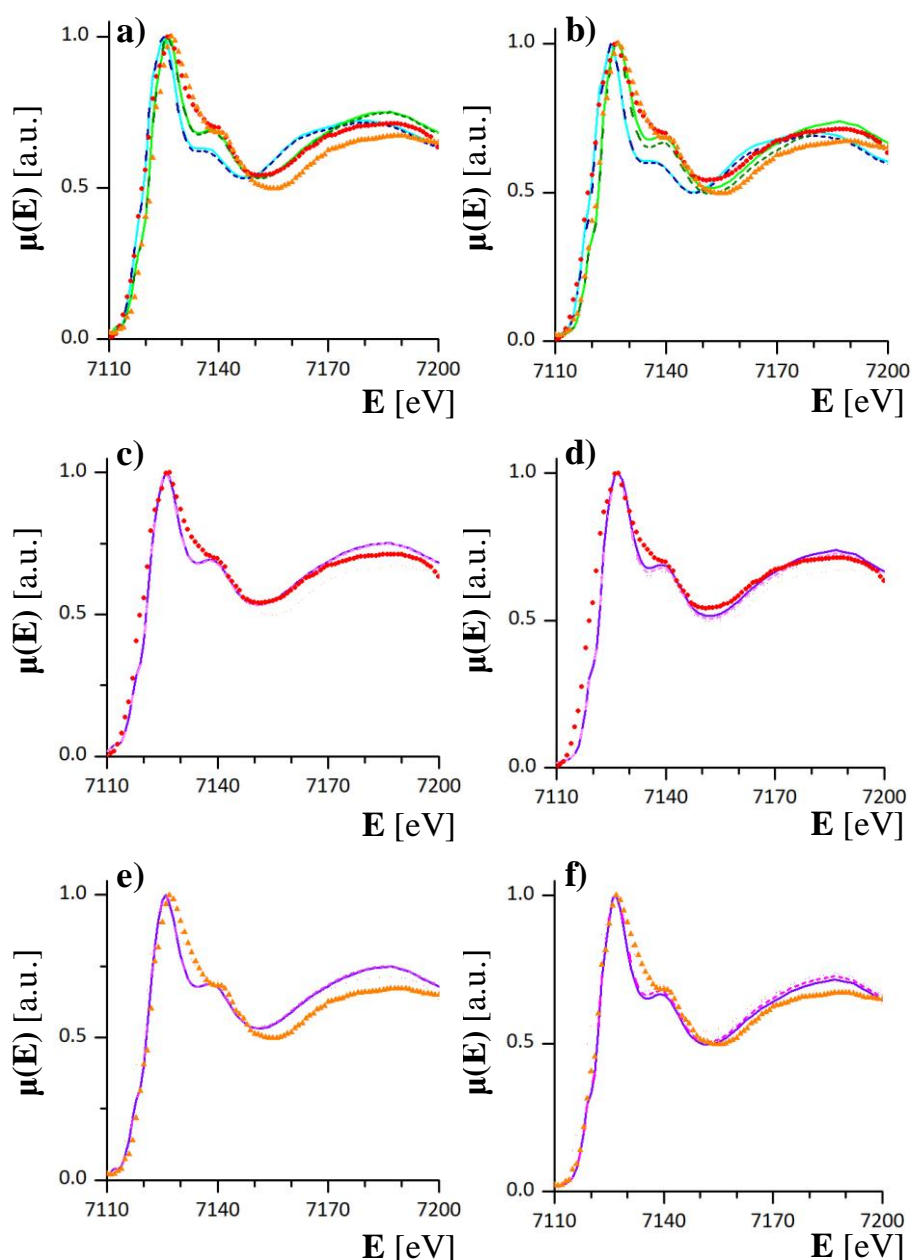[b]Q_{SWy} is calculated using Eq. 1 for EXAFS and Eq. 2 for XANES.

Figure 4. Experimental XANES spectra (red circles for Milos- and orange triangle for SWy-montmorillonite) of montmorillonite with iron incorporation and modeled XANES spectra (lines) of Fe incorporated in the octahedral layer of 2:1 clay. In panels a and b, blue colors correspond to the incorporated ferrous iron (Fe2+), while green colors represent incorporated ferric iron (Fe3+). The lines with lighter color represent the iron at the cis-site while dashed darker lines correspond to the trans-occupational site. In panels c−f, the lines represent the linear combination fits, the darker purple lines show Fit 1, while the dashed lighter pink lines correspond to the Fit 2. Panels c and d represent fits to the Milos-montmorillointe spectra with contributions determined in Table 1, while panels e and f show linear combination fit for SWy-montmorillonite spectra with contributions determined in Table 2. The calculated XANES spectra for panels a, c, and e were derived from MD simulations, while for panels b, d, and f, the relaxed structures served as a basis.

3.2. XANES spectra

Fe K-edge XANES spectra based on the RSMS approach for montmorillonite with Fe^{2+} and Fe^{3+} located in the *cis-* and *trans*-occupational sites were obtained and compared with the experimental spectrum (Figure 3). At a first glance, the simulation and the measurement results seem to agree, the characteristic shoulder at about 7140 eV of the main peak is over predicted (Figure 3). A more clear difference can be seen in the pre-edge region where the experimental spectrum shows only a smooth shoulder but the RSMS calculations predict sharp pre-edges.
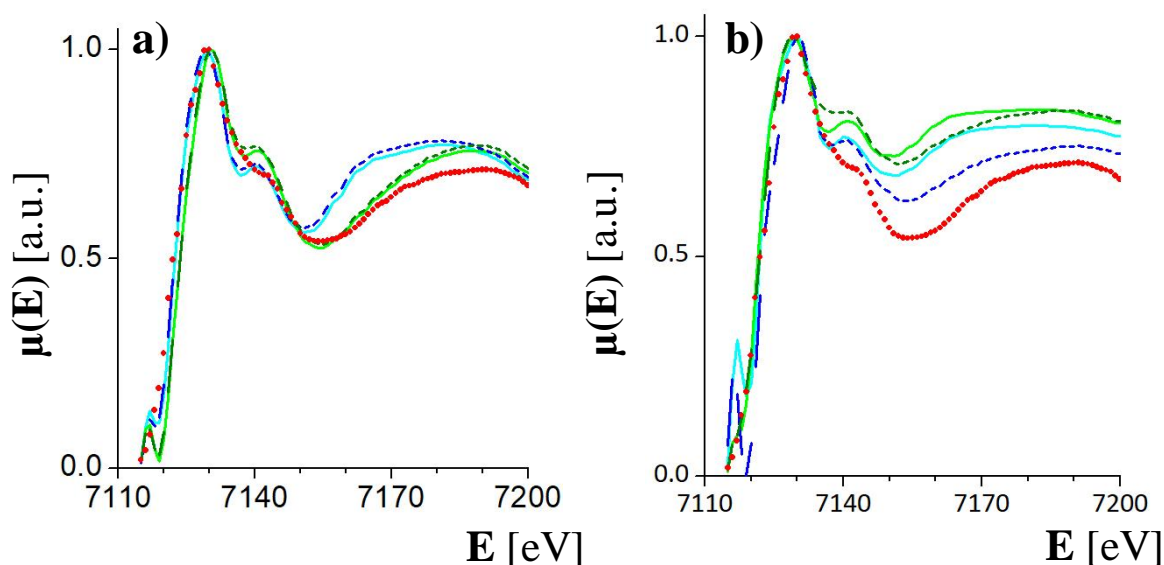
Figure 3. Experimental XANES spectra (red circles) of montmorillonite with iron incorporation and *ab initio* XANES spectra (lines) of Fe incorporated in the octahedral layer of 2:1 clay applying FEFF 8.40 software. Blue colors correspond to the incorporated ferrous iron (Fe^{2+}) while green colors represent incorporated ferric iron (Fe^{3+}). The lighter straight lines represent the Fe at the *cis*-site while dashed darker lines correspond to the *trans*-occupational site. The XANES spectra for *a)* were derived from the relaxed structures while for *b)* the MD simulations served as a basis.

The contradictions in the XANES spectra obtained with FEFF 8.40 software suggest that another, more sophisticated theoretical method should be applied. Therefore, we also calculated the XANES spectra based on the fully relativistic DFT-LSDA method for the four different structures with relaxed geometries using the FDMNES software[49]. The calculated spectra agreed well with both the measured XANES of the Milos- and the SWy-montmorillonite samples, however, the spectra obtained for Fe^{2+} and Fe^{3+} are clearly different (Figure 4a,b). The shape of the first edge of the XANES spectra for Fe^{2+} and Fe^{3+} are very

similar, only a small energy shift (1-2 eV) can be recognized. The height of the characteristic shoulder at about 7135 eV demonstrates more clearly the difference between Fe^{2+} and Fe^{3+} (Figure 4a,b). This shoulder is also clearly seen in the experimentally measured spectra and its height is closer to the one of Fe^{3+} (Figure 4a,b). The structural coordination environment (*cis*- and *trans*-site) of the Fe octahedron seems to have little effect on the calculated spectra that agrees well with the previous EXAFS studies.

The oxidation state and the preferential occupational site of the substituted iron atoms were determined using the linear combination fit defined as in Eq. 2. The data can be fitted best as a linear combination ("*Fit 1*") of Fe^{2+}_{Cis}, Fe^{2+}_{Trans}, Fe^{3+}_{Cis} and Fe^{3+}_{Trans} (Table 1 and 2). The corresponding compounds of the fits agreed best within the margin of errors. The exclusive contribution of the calculated Fe^{3+}_{Cis} spectrum in the linear combination fit to measured Milos-montmorillonite spectrum ensured that ferric iron is preferred in the bulk incorporation. As the XANES spectra of the SWy-montmorillonite is very similar to the Milos-montmorillonite (with a nearly identical shoulder at the right side of the first peak), the exclusive ferric iron contribution is expected. The differences can be seen in the post-edge region cannot be reproduced assuming random distribution of the iron atoms in the sample.

A "*Fit 2*" was also performed similarly to the EXAFS case when the total contributions of the Fe^{2+} and Fe^{3+} were kept the same but the contributions of the different occupational sites were equalized (Table 1 and 2) to test the contribution of the different occupational site. The comparison of the fitting quality (Table 1 and 2) and the fitted curves (Figure 4c-f) revealed that there were only small differences between the two fits. Therefore, the preferential occupation of *cis*- or *trans*-sites by Fe^{2+} and Fe^{3+} in montmorillonite could not be inferred from the XAFS spectra alone.

3.3. Structural position of Fe in bulk montmorillonite

The structural parameters of the relaxed structures from geometry optimization were compared with the measurement results to obtain information about the differences between the different structures (Table 3). The average $Fe^{2+} - O$ distances of (2.13 ± 0.03) Å are longer than the $Fe^{3+} - O$ distances of (2.03 ± 0.03) Å. The calculated distances are nearly identical for the *cis*- and *trans*-sites. The Fe – Al and Fe – Si distances are identical for Fe^{2+} and Fe^{3+} (Table 3). Therefore, the Fe-O shell provides only a hint about the oxidation state, whereas any conclusions about the *cis*- or *trans*-occupation based on the structural data are highly speculative.

354 **Table 3.** Structural parameters and energy difference of bulk montmorillonite with iron
355 incorporation derived from the *ab initio* calculations and EXAFS measurements

Structural parameters		Fe^{2+}		Fe^{3+}		EXAFS (Milos) "*Fit 1*"	Measurement (Milos)
		Cis	*Trans*	*Cis*	*Trans*		
Fe−O$_{All}$[a]	CN [-]	6.0 ± 0.1	6.0 ± 0.1	6.0 ± 0.1	6.0 ± 0.1	6.0 ± 0.1	5.8 ± 0.4
	R [Å]	2.14 ± 0.03	2.12 ± 0.03	2.03 ± 0.03	2.02 ± 0.03	2.05 ± 0.03	2.01 ± 0.01
Fe−O$_{H}$[b]	CN [-]	2.0 ± 0.1	2.0 ± 0.1	2.0 ± 0.1	2.0 ± 0.1	2.0 ± 0.1	
	R [Å]	2.08 ± 0.04	2.10 ± 0.04	2.00 ± 0.04	2.01 ± 0.04	2.03 ± 0.04	
Fe−O[c]	CN [-]	4.0 ± 0.1	4.0 ± 0.1	4.0 ± 0.1	4.0 ± 0.1	4.0 ± 0.1	
	R [Å]	2.14 ± 0.03	2.13 ± 0.03	2.04 ± 0.02	2.03 ± 0.02	2.07 ± 0.02	
Fe−Al	CN [-]	3.0 ± 0.1	3.0 ± 0.1	3.0 ± 0.1	3.0 ± 0.1	3.0 ± 0.1	2.8 ± 0.5
	R [Å]	3.04 ± 0.03	3.04 ± 0.03	3.07 ± 0.03	3.07 ± 0.03	3.06 ± 0.03	3.05 ± 0.02
Fe−Si	CN [-]	4.0 ± 0.1	4.0 ± 0.1	4.0 ± 0.1	4.0 ± 0.1	4.0 ± 0.1	3.8 ± 0.6
	R [Å]	3.25 ± 0.03	3.23 ± 0.03	3.24 ± 0.03	3.22 ± 0.03	3.23 ± 0.03	3.25 ± 0.03
Energy difference [kcal/mol]		0.0 ± 0.5		0.0 ± 0.5		—	—

[a]O$_{all}$ corresponds to the all oxygen atoms in the first shell
[b]O$_H$ corresponds to the oxygen atoms of OH$^-$ groups in the first shell
[c]O corresponds to the oxygen atoms (not member of OH$^-$ groups) in the first shell

356 The occupancy of the *cis-* and *trans-*sites can be evaluated based on the relative energies of Fe
357 substitution in the *cis-* and *trans-*octahedra. The calculations predict that for low Fe content
358 investigated in this study, the relative energies of iron (both Fe^{2+} and Fe^{3+}) in *cis-* and *trans-*
359 sites are equal within the uncertainties of the calculations (Table 3). This means that iron is
360 randomly distributed between the *cis-* and *trans-*sites. The observation is consistent with the
361 very similar structural parameters obtained in the XAFS simulations.
362 A previous *ab initio* study showed the differences between ferrous and ferric iron bearing
363 smectites investigating their structural properties (local structure of iron, hydroxyl
364 orientations, vibration dynamics of H and Si)[59]. Our calculated structural parameters showed
365 good agreement with the results of this study[59]: the average Fe – O bond lengths (2.11 Å and
366 2.02 Å) agreed within the uncertainty and Fe substitutions did not affect the coordination
367 structures of the Al – O and Si – O polyhedral in neither studies[59].

4. Implication of the theoretical study in the interpretation of XAFS

This study demonstrates that the full XAFS spectra of natural montmorillonites can be obtained as a linear combination fit of theoretical ab initio XAFS spectra calculated based on ab initio MD trajectories for pure phases without any empirical adjustments of structural parameters such as bond distances or coordination. Performed linear combination analysis yields valuable information on the mechanism of structural incorporation of Fe in natural clay minerals. The comparison of two different theoretical approaches for XAS calculations (RSMS and DFT-LSDA) demonstrates that XANES calculations for elements with *3d-* electrons largely depends on the used theory. The differences between predictions of the two methods are significant and influence the accuracy of the quantitative data analysis. The results of the linear combination fit of XANES spectra obtained based on the DFT-LSDA approach showed best agreement with the corresponding analysis of the EXAFS spectra. The quantitative analysis of both EXAFS and XANES spectra suggest that iron is predominantly present in bulk montmorillonite in Fe^{3+} oxidation state. The experimental spectra could be fitted equally well by assuming arbitrary contribution of Fe in *cis-* and *trans-*sites or imposing equal occupation of these sites. The energy calculations suggested that at low concentrations Fe^{2+} and Fe^{3+} are equally distributed between *cis-* or *trans-*sites.

An important step towards is the better understanding of the iron uptake mechanism in the determination of relevant edge surfaces of montmorillonite. Such information will be essential for understanding the mechanism of the probable oxidative uptake of iron (Fe^{2+}_{aq} -> Fe^{3+}_{surf}) by clay minerals[9]. In the best case, the comparison of the *ab initio* based XAFS calculations and the measurements will result in the determination of the oxidation state of Fe in the bulk and at the surface. The results may give insight on whether the Fe^{2+} -> Fe^{3+} redox reaction occurs between the Fe atoms adsorbed on the surface and incorporated structurally into the bulk.

5. Acknowledgements

409 **References**

(1) Stucki, J. W.; Goodman B. A.; Schwertamann, U. Iron in soils and clay minerals. *Springer Science & Business Media*, Dordrecht, Netherlands, **2012**, vol. 217, pp. 1-3.

(2) Ilton, E. S.; Boily, J. F.; Buck, E. C.; Skomurski, F. N.; Rosso, K. M.; Cahill, C. L.; Bargar, J. R.; Felmy, A. R. Influence of dynamical conditions on the reduction of U(VI) at the magnetite-solution interface. *Environ. Sci. Technol.* **2010**, *44*, 170-176.

(3) Soltermann, D.; Fernandes, M. M.; Baeyens, B.; Miehé-Brendlé, J.; Dähn, R. Competitive Fe(II)−Zn(II) uptake on a synthetic montmorillonite. *Environ. Sci. Technol.* **2014**, *48*, 190-198.

(4) Leupin, O. X.; Birgersson, M.; Karnland, O.; Korkeakoski, P.; Sellin, P.; Mäder, U.; Wersin, P. Montmorillonite stability under near-field conditions. *Technical Report 14-12, National Cooperative for the Disposal of Radioactive Waste (NAGRA)*, Wettingen, Switzerland, **2014**, pp. 37-38.

(5) Stucki, J. W.; Golden, D. C.; Roth, C. B. Effects of reduction and reoxidation of structural iron on the surface charge and dissolution of dioctahedral smectites. *Clay. Clay. Miner.* **1984**, *32(5)*, 350-356.

(6) Hofstetter, T. B.; Schwarzenbach, R. P.; Haderlein, S. B. Reactivity of Fe(II) species associated with clay minerals. *Environ. Sci. Technol.* **2003**, *37*, 519-528.

(7)   Hofstetter, T. B.; Neumann, A.; Schwarzenbach, R. P. Reduction of nitroaromatic compounds by Fe(II) species associated with iron-rich smectites. *Environ. Sci. Technol.* **2006**, *40*, 235-242.

(8)   Stucki, J. W.; Lee, K.; Zhang, L.; Larson, R. A. Effects of iron oxidation state on the surface and structural properties of smectites. *Pure. Appl. Chem.* **2002**, *74 (11)*, 2145-2158.

(9)   Soltermann, D.; Fernandes, M. M.; Baeyens, B.; Dähn, R.; Joshi, P. A.; Scheinost, A. C.; Gorski, C. A. Fe(II) uptake on natural montmorillonites. I. Macroscopic and spectroscopic characterization. *Environ. Sci. Technol.* **2014**, *48*, 8688-8697.

(10)   Pfingsten, W.; Bradbury, M. H.; Baeyens, B. The influence of Fe(II) competition on the sorption and migration of Ni(II) in MX-80 bentonite. *Appl. Geochem.* **2014**, *26*, 1414–1422.

(11)   Soltermann, D.; Baeyens, B.; Bradbury, M. H.; Fernandes, M. M. Fe(II) uptake on natural montmorillonites. II. Surface complexation modeling. *Environ. Sci. Technol.* **2014**, *48*, 8698-8705.

(12)   Guggenheim, S.; Adams, J. M.; Bain, D. C.; Bergaya, F.; Brigatti, M. F.; Drits, V. A.; Formosso, M. L. L.; Galan, E., Kogure, T.; Stanjek, H. Summary of recommendations of nomenclature committees relevant to clay mineralogy: Report of the association internationale pour l'Etude des Argiles (AIPEA) nomenclature committee for 2006. *Clay. Clay. Miner.* **2006**, *54 (6)*, 761-772.

(13)   Tsipursky, S. I.; Drits, V. A. The distribution of octahedral cations in the 2:1 layers of dioctahedral smectites studied by oblique-texture electron diffraction. *Clay. Miner.* **1984**, *19*, 177-193.

(14)   Cardile, C. M. Structural site occupation of iron within 2:1 dioctahedral phyllosilicates studied by57Fe Mössbauer spectroscopy. *Hyperfine. Interact.* **1988**, *41(1)*, 767-770.

(15)   Stucki, J. W. Properties and behaviour of iron in clay mineral in *Handbook of Clay Science* (editors: Bergaya, F.; Theng, B. K. G.; Lagaly, G.) **2006**, pp. 424-430.

(16)   Cardile, C. M.; Johnston, J. H. [57]Fe Mössbauer spectroscopy of montmorillonites: A new interpretation. *Clay. Miner.* **1986**, *34(4)*, 307-313.

(17)   Manceau A., Lanson B., Drits V. A., Chateigner D., Gates W. P., Wu J., Huo D., Stucki J. W. Oxidation-reduction mechanism of iron in dioctahedral smectites: I. Crystal chemistry of oxidized reference nontronites. *Am. Mineral.* **2000**, *85*, 133-152.

(18) Tsipursky, S. I.; Drits, V. A. The distribution of octahedral cations in the 2:1 layers ofdioctahedral smectites studied by oblique-texture electron diffraction. *Clay. Miner.* **1984**, *19*, 177-193.

(19) Gorski, C. A.; Aeschbacher, M.; Soltermann, D.; Voegelin, A.; Baeyens, B.; Fernandes, M. M.; Hofstetter, T. B.; Sander, M. Redox properties of structural Fe in Clay Minerals. 1. Electrochemical quantification of electron-donating and -accepting capacities of smectites. *Environ. Sci. Technol.* **2012**, *46*, 9360-9368.

(20) Gorski, C. A.; Klüpfel, L.; Voegelin, A.; Sander, M.; Hofstetter, T. B. Redox properties of structural Fe in clay minerals. 2. Electrochemical and spectroscopic characterization of electron transfer irreversibility in ferruginous smectite, SWa‑1. *Environ. Sci. Technol.* **2012**, *46*, 9369−9377.

(21) Gorski, C. A.; Klüpfel, L. E.; Voegelin, A.; Sander, M.; Hofstetter, T. B. Redox properties of structural Fe in clay minerals: 3. Relationships between smectite redox and structural properties. *Environ. Sci. Technol.* **2013**, *47*, 13477−13485.

(22) Soltermann, D.; Fernandes, M. M.; Baeyens, B.; Dähn, R.; Miehé-Brendlé, J.; Wehrli, B.; Bradbury, M. H. Fe(II) sorption on a synthetic montmorillonite. A combined macroscopic and spectroscopic study. *Environ. Sci. Technol.* **2013**, *47*, 6978-6986.

(23) Churakov, S. V.; Dähn, R. Zinc adsorption on clays inferred from atomistic simulations and EXAFS spectroscopy. *Environ. Sci. Technol.* **2012**, *46*, 5713-5719.

(24) Ladeira, A. C. Q.; Ciminelli, V. S. T.; Duarte, H. A.; Alves, M. C. M.; Ramos, A. Y. Mechanism of anion retention from EXAFS and density functional calculations: Arsenic (V) adsorbed on gibbsite. *Geochim. Cosmochim. Ac.* **2001**, *65 (8)*, 1211-1217.

(25) Shermann, D. M.; Randall, S. R. Surface complexation of arsenic(V) to iron(III) (hydr)oxides: Structural mechanism from ab initio molecular geometries and EXAFS spectroscopy. *Geochim. Cosmochim. Ac.* **2003**, *67 (22)*, 4223-4230.

(26) Tsutsui, Y.; Sugimoto, K.-i.; Wasada, H.; Inada, Y.; Funahashi, S. EXAFS and ab initio molecular orbital studies on the structure of solvated silver(I) ions. *J. Phys. Chem. A.* **1997**, *101*, 2900-2905.

(27) Bocharov, D.; Krack, M.; Kalinko, A.; Purans, J.; Rocca, F.; Ali, S. E.; Kuzmin, A. Ab initio molecular dynamics simulations of the Sc K-edge EXAFS of scandium triuoride. *J. Phys. Conf. Ser.* **2015**, *712*, 012009.

(28) Bocharov, D.; Chollet, M.; Krack, M.; Bertsch, J.; Grolimund, D.; Martin, M.; Kuzmin, A.; Purans, J.; Kotomin, E. Interpretation of the U L3-edge EXAFS in uranium dioxide using molecular dynamics and density functional theory simulations. *J. Phys. Conf. Ser.* **2016**, *712*, 012091.

(29) Teo, B. K. EXAFS: Basic principles and data analysis. *Springer* **1986**, vol. 9, pp. 21-23.

(30) Churakov, S. V. Ab initio study of sorption on pyrophyllite: Structure and acidity of the edge sites. *J. Phys. Chem. B* **2006**, *110*, 4135-4146.

(31) Churakov, S. V.; Kosakowski, G. An ab initio molecular dynamics study of hydronium complexation in Na-montmorillonite. *Philos. Mag.* **2010**, *90 (17)*, 14-28.

(32) Krähenbühl, F.; Stöckli, H. F.; Brunner, F.; Kahr, G.; Müller-Vonmoos, M. Study of the water-bentonite system by vapour adsorption, immersion calorimetry and X-ray techniques: I. Micropore volumes and internal surface areas, following Dubinin's theory. *Clay. Miner.* **1987**, *22*, 1-9.

(33) Johnston, J. H.; Cardile, C. M. Iron substitution in montmorillonite, illite and glaucionite by [57]Fe Mössbauer spectroscopy. *Clay. Clay. Miner.* **1987**, *35 (3)*, 170-176.

(34) CP2K developers group, http://www.cp2k.org (2000-2017)

(35) VandeVondele, J.; Krack, M.; Mohamed, F.; Parrinello, M.; Chassaing, T.; Hutter, J. QUICKSTEP: Fast and accurate density functional calculations using a mixed Gaussian and plane waves approach. *Comput. Phys. Commun.* **2005**, *167*, 103-128.

(36) Goedecker, S.; Teter, M.; Hutter, J. Separable dual-space Gaussian pseudopotentials. *Phys. Rev. B* **1996**, *54 (3)*, 1703-1710.

(37) Krack, M. Pseudopotentials for H to Kr optimized for gradient-corrected exchange-correlation functionals. *Theor. Chem. Acc.* **2005**, *114*, 145-152.

(38) VandeVondele, J.; Hutter, J. Gaussian basis sets for accurate calculations on molecular systems in gas and condensed phases. *J. Chem. Phys.* **2007**, *127*, 114105.

(39) Perdew, J. P.; Burke, K.; Ernzerhof, M. Generalized gradient approximation made simple. *Phys. Rev. Lett.* **1996**, *77 (18)*, 3865-3868.

(40) Perdew, J. P.; Burke, K.; Ernzerhof, M. ERRATA: Generalized Gradient Approximation Made Simple [Phys. Rev. Lett. 77, 3865 (1996)]. *Phys. Rev. Lett.* **1997**, *78 (7)*, 1396.

(41) Rollmann, G.; Rohrbach, A.; Entel, P.; Hafner, J. First-principles calculation of the structure and magnetic phases of hematite. *Phys. Rev. B* **2004**, *69*, 165107.

(42) Liechtenstein, A. I.; Anisimov, V. I.; Zaanen, J. Density-functional theory and strong interactions: Orbital ordering in Mott-Hubbard insulators. *Phys. Rev. B* **1995**, *52 (8)*, R5467-R5470.

(43) Dudarev, S. L.; Botton, G. A.; Savrasov, S. Y.; Humphreys, C. J.; Sutton, A. P. Electron-energy-loss spectra and the structural stability of nickel oxide: An LSDA+U study. *Phys. Rev. B* **1998**, *57 (3)*, 1505-1509.

(44) Bussi, G.; Donadio, D.; Parrinello, M. Canonical sampling through velocity rescaling. *J. Chem. Phys.* **2007**, *26*, 014101.

(45) Ankudinov, A. L.; Ravel, B.; Rehr, J. J.; Conradson, S. D. Real-space multiple-scattering calculation and interpretation of X-ray absorption near-edge structure. *Phys. Rev. B* **1998**, *58 (12)*, 7565-7575.

(46) Ankudinov, A. L.; Nesvizhskii, A. I.; Rehr J. J. Dynamic screening effects in x-ray absorption spectra. *Phys. Rev. B* **1998**, *67*, 115120

(47) Ankudinov, A. L.; Rehr, J. J. Theory of solid-state contributions to the X-ray elastic scattering amplitude. *Phys. Rev. B* **2000**, *62 (4)*, 2437-2445

(48) Rehr, J. J.; Ankudinov, A. Ravel B. User's Guide, FEFF v8.40. University of Washington, Seattle, United States, **2006**.

(49) Bunau, O.; Joly, Y. Self-consistent aspects of X-ray absorption calculations. *J. Phys.-Condens. Mat.* **2009**, *21*, 345501.

(50) Guda, S. A.; Guda, A. A.; Soldatov, M. A.; Lomachenko, K. A.; Bugaev, A, L.; Lamberti, C.; Gawelda, W.; Bressler, C.; Smolentsev, G.; Soldatov, A. V.; Joly, Y. Optimized finite difference method for the full-potential XANES simulations: Application to molecular adsorption geometries in MOFs and metal-ligand intersystem crossing transients. *J. Chem. Theory. Comput.* **2015**, *11*, 4512-4521.

(51) Amestoy, P. R.; Guermouche, A.; L'Excellent, J.-Y.; Pralet, S. Hybrid scheduling for the parallel solution of linear systems. *Parallel. Comput.* **2006**, *32 (2)*, 136-156.

(52) Joly Y. FDMNES User's Guide, Grenoble, France, **2016**, pp. 49-53.

(53) Vantelon, D.; Montarges-Pelletier, E.; Michot, L. J.; Briois, V.; Pelletier, M.; Thomas, F. Iron distribution in the octahedral sheet of dioctahedral smectites. An Fe K-edge X-ray absorption spectroscopy study. *Phys. Chem. Miner.* **2003**, *30*, 44-53.

(54) Newville, M. IFFEFFIT: interactive XAFS analysis and FEFF fitting. *J. Synchrotron. Radiat.* **2001**, *8*, 322-324.

(55) Ravel, B.; Newville, M. ATHENA, ARTEMIS, HEPHAESTUS: Data analysis for X-ray absorption spectroscopy using IFEFFIT. *J. Synchrotron. Radiat.* **2005**, *12*, 537-541.

(56) Teo, B. K. EXAFS: Basic principles and data analysis. *Springer* **1986**, vol. 9, pp. 114-128.

(57) Koningsberger, D.C.; Prins, R. X-Ray Absorption: Principles, Applications, Techniques of EXAFS, SEXAFS and XANES. John Wiley & Sons, New York, USA, **1988**, Chapter 6, pp. 211-253.

(58) Schaefer, M. V.; Gorski, C. A.; Scherer, M. M. Spectroscopic evidence for interfacial Fe(II)-Fe(III) electron transfer in a clay mineral. *Environ. Sci. Technol.* **2011**, *45 (2)*, 540-545.

(59) Liu, X.; Meijer, E. J.; Lu, X.; Wang, R. Ab initio molecular dynamics study of Fe-containing smectites. *Clay. Clay. Miner.* **2010**, *58 (1)*, 89-96.